Thermal conduction in three-dimensional printed porous samples by high resolution infrared thermography

D. Muñoz Codorníu, J.J. Moyano, M. Belmonte, M.I. Osendi, P. Miranzo[*]

Instituto de Cerámica y Vidrio, CSIC, Campus de Cantoblanco, 28049, Madrid, Spain

A B S T R A C T

The thermal conductivity (κ) is a key parameter that defines many of the technological uses of three-dimensional (3D) porous architectures. Despite the variety of methods for determining κ, problems generally arise when researchers try to apply them to cellular materials and 3D structures. The present work proposes an affordable lab-made device for analysing anisotropic heat flow in 3D porous architectures via high resolution infrared thermography. The method is validated using dense materials of known thermal conductivity. Temperature gradients measured for porous specimens have been correlated to the thermal conductivity estimated from a simple resistors model, assessing the main factors that affect the experimental measurements. The porous specimens of SiC, MAX-phase and graphene-based nanostructures are in-house manufactured by direct ink writing (robocasting).

1. Introduction

Thermal conductivity is the main parameter governing the heat transfer that determines many of the technological uses of materials, especially in thermal management, energy harvesting and thermal energy storage (TES) applications. The measurement of the thermal conductivity can be problematic when dealing with highly porous materials, in particular, for three-dimensional (3D) architectures manufactured by using a printing process from computer-aided designs (CAD). These types of complex structures have application in various fields where heat dissipation is a fundamental matter [1,2], for example, in catalysis [3–5], energy storage and production [6,7], and heat exchangers and heat sinks [8,9]. The effect of the printing parameters on the thermal properties of 3D printed structures has been treated in several studies focused on polymers and metal structures processed by fused deposition modelling (FDM) [10–15], but only relatively few works have dealt with 3D ceramic structures.

A great variety of methods for determining the thermal conductivity are based on monitoring temperature changes produced during sample heating, obtaining the thermal diffusivity (α) and conductivity (κ) with distinct precision levels that depend on the selected method. In the case of porous materials, each pore represents a small volume filled with gas (air), a medium of very low thermal conductivity (0.023 W m^{-1} K^{-1} under normal conditions of pressure and temperature [16]), which generates notable heterogeneities that complicate the κ measurement.

Moreover, since the external surfaces for these materials are usually very rough, contact thermal resistances become an additional problem. The present work uses a lab-made device for measuring temperature profiles generated in 3D porous architectures placed between two heating sources with an infrared (IR) camera, examining the pros and cons of this straightforward testing gadget.

2. Thermal conductivity methods

The methods for measuring the thermal conductivity of materials can be classified according to the sample temperature distribution as steady-state or transient heat flow methods. The most common methods are compared in some recent reviews [17,18].

Steady-state heat flow methods are generally based on inducing a constant unidirectional temperature gradient across the sample. In this way, samples are arranged between a hot source and a cold sink, while they are thermally insulated from their surroundings. This allows simplifying the Fourier's conduction equation in partial derivatives to the following expression:

$$\frac{\partial^2 T}{\partial z^2} = 0 \tag{1}$$

where z coincides with the heat flow direction. In the case of perfect insulation, the temperature profiles in the sample will be linear in the

---

heat flow direction and constant in the perpendicular planes. Accordingly, the thermal conductivity is calculated from the temperature gradient in the specimen and the heat flowing through a certain section of the sample. In practice, these procedures are subdivided into two types: absolute and comparative. In absolute methods, the thermal power transferred to the sample is known; whereas in comparative methods, the test sample and one or more reference specimens of known conductivity are stacked parallel to the heat flow direction. The unknown thermal conductivity is, then, obtained by comparing gradients measured in the test sample and the reference materials, assuming the same heat flux through the samples in contact. The achievement of a unidirectional heat flow is one of the main issues for both absolute and comparative methods. For that purpose, guard rings around the temperature measurement zone are usually employed, which normally consist of thermally insulating materials with a series of lateral electrical resistances that reproduce a temperature gradient similar to the reached in the measuring stacking to avoid/reduce lateral heat losses.

The most widely used steady-state methods for porous materials are the guarded hot plate (ASTM C177-13), valid for materials with very low thermal conductivity ($\kappa < 1$ W m^{-1} K^{-1}); the guarded-comparative-longitudinal heat flow meter (ASTM-1225), limited for materials with conductivities higher than ~ 1 W m^{-1} K^{-1}; and also a modification of the latter (ASTM D5470-17) that consists of measuring the thermal resistance of the material as a function of the specimen thickness when the use of thermocouples is not possible. These procedures have all in common the easiness of the fundamental equations, the high precision, and the advantage of a simple sample geometry (cylinder or square prism); however, the usually long stabilization times (up to 24 h) to get steady-state conditions and large sample size requirements are some of the limitations (typically specimens are up to 5 cm high and 5-50 cm diameter for cylinders or side length for square prism specimens). In addition, there are some additional problems like the imperfect insulation and the often tricky attachment of the thermocouples. The situation gets worse in the case of porous samples. On the one hand, the surface of a porous material is quite irregular, which prevents intimate contact between the specimen and the heat sources and thermocouples and, on the other hand, uncounted heat losses and imprecise measurements of the thermal gradients may occur. Additionally, for comparative methods, the contact thermal resistances between the reference and test samples are of paramount importance, quite more relevant than for dense samples of smoother surface. Finally, the lower thermal conductivity of porous materials further increases the time required for the thermal stabilization.

Transient methods monitor the temporal evolution of the temperature after the sample heating for a time period in the order of seconds. For this reason, although the thermal insulation is still necessary, the heat losses to the environment are less significant than in the steady-state methods. The thermal conductivity calculation is indirectly carried out since most of these methods usually determine the thermal diffusivity and calculate the conductivity from the material's bulk density (ρ) and the specific heat (c_p) using the expression $\kappa = \alpha \cdot \rho \cdot c_p$. The higher the diffusivity, the faster the medium responds to temperature changes. Some methods use a wire or plate embedded between two similar specimens of the same material for Joule effect heating; the most widely employed are the hot wire (HW, ASTMC1113) and the transient plane source (TPS, ISO 22007-2) techniques. A close contact between the heat sources and the specimens is required in both methods. On the other hand, a laser pulse is used to heat one of the specimen faces in the laser flash method (ASTM E-1461); hence, a real contact between the heat source and the sample is avoided. Recently, the TPS method has been modified (MTPS, ASTM D7984-16) by means of a flat heater/sensor and a guard ring to use only one specimen and, therefore, a single interface, which practically ensures a one-dimensional heat transfer.

The main advantages of the transient methods are the reduced heat losses, the smaller sample size, and the wide range of measurable conductivities, from 0.02 to more than 2000 W m^{-1} K^{-1} depending on the method, with reasonable accuracies (1–5%) [17,18]. In general, the transient methods allow handling samples of sizes that vary from ~ 5 cm in height and 100–200 cm^2 in section, in the case of hot wire, to ~ 2 mm in height and sections of ~ 1.3 cm^2 for the laser flash technique. However, specific problems arise regarding their applicability to cellular materials and 3D structures. The hot wire and the transient plane source methods present similar problems linked to the normally poor contact between the heat source and the specimen. As for the laser flash method, its applicability to these materials is questionable because the laser beam would impact directly the infrared detector without interfering with the sample at all.

In the case of 3D printed structures, some thermal conductivity studies can be found for polymers fabricated by FDM that employ either the TPS method [10,11] or simple longitudinal heat flow meter method [12–15]. The latter one consists of one heat source and one heat sink, two metal bars, generally copper, between them and the test specimen in the centre of the assembly. Several temperature sensors are inserted in the top and bottom metal bars for measuring the temperature gradient and, accordingly, not only the sample but the two contact resistances are included in this measurement. From the thermal impedance (sum of the thermal resistance of the material and all contact resistances) measurements in various specimens of different thickness (between 4 and 10 mm), the effect of the interfacial thermal resistances can be eliminated, and, hence, the thermal conductivity can be estimated. The specimen section varies between 25 × 25 and 40 × 40 mm^2, thus, similar to those used in TPS. Regarding additively manufactured 3D ceramic structures, to the best of the authors knowledge, there are no experimental works analysing their thermal conductivities, although comparative evaluations of the heat dissipation capability of different printed materials during cooling have recently been addressed [19–22].

3. Materials description and thermal conduction procedure

3.1. Materials

Dense and porous materials were selected for the study. Dense cylinders of commercial materials of known thermal conductivity were used to validate the method here proposed (see section 3.2), whereas the porous specimens were in-house manufactured by direct ink writing (robocasting). Robocasting is an additive manufacturing technique that allows printing 3D materials from highly concentrated inks containing certain amount of organic additives to gain control over the ink viscosity and rheology. The proper ink is extruded through a needle, typically of diameter between 250 and 800 μm, following a previously computer-designed pattern [23].

Reference standards of Pyrex® 7740, Pyroceram® 9606, and alumina (NIST SRM 720) of certified thermal conductivity were selected as dense materials, although their thermal conductivities were also measured using the laser flash method. Pyrex® is a low-thermal-expansion borosilicate glass (SiO_2 and B_2O_3, with small amounts of Na_2O and Al_2O_3) developed by Corning Inc. with a certified κ of 1.1 W m^{-1} K^{-1} at room temperature. Pyroceram® 9606 is a magnesium aluminium silicate glass-ceramic with TiO_2 as nucleating agent, also developed by Corning Inc.; its thermal conductivity is 4.1 W m^{-1} K^{-1} at room temperature, which is higher than κ of Pyrex®. The last material is a standard alumina of significantly higher thermal conductivity (33 W m^{-1} K^{-1}). These samples are discs of 12.7 mm diameter and 2 mm thick.

The specimens printed by robocasting are three-dimensional structures with a netlike interior formed by layers of parallel rods of diameter "Ø", with an in-plane separation "a", and orthogonally stacked in z-direction (Fig. 1a). The distance between consecutive layers with the same rod orientation (h) is below twice the rod diameter to assure some rod overlapping and a good contact between rods in z-direction (h/2Ø = π/4 in the present designs). The printed structures have a frame that contours the scaffolding providing additional support, as it can be clearly seen in Fig. 1b where an optical view of one representative printed structure is
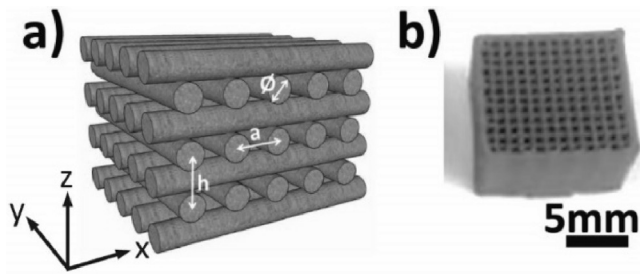
Fig. 1. (a) Schematic draw of the inside scaffolding design with indication of the characteristic lattice parameters (the rod diameter (Ø), in-plane separation between rods (a), and distance between consecutive layers with same rod orientation (h)); and (b) optical image of a representative real printed structure, corresponding to SiC$_{50}$-7, where the frame can be clearly observed.

shown. The cell parameters define the macro-porosity of the structures,

$\pi_{macro} = \left(1 - \frac{\pi \cdot \varnothing^2}{2 \cdot a \cdot h}\right) - V_{Frame}/V_{Total}$[24]. After printing, the structures

were usually heat treated at temperatures in the 415–600 °C range to remove the organic additives of the ink and, subsequently, densified at the corresponding sintering temperature to improve the particle contacts and the mechanical performance of the material. Besides the macro-pores associated to the designed hollow cells that are clearly observed in Fig. 1b, additional porosity may remain inside the rods (π_{rod}), which is determined from π_{macro} and the total porosity, given by the measured geometrical density and the theoretical density of the rod material. This porosity can be observed in the images (Fig. 2) taken by scanning electron microscopy (SEM).

Three distinct 3D materials were tested, in particular, two ceramics that corresponded to silicon carbide (SiC) and Cr$_2$AlC MAX-phase specimens, and a composite consisting of reduced graphene oxide nanoplatelets (rGO) and a cross-linked preceramic polymer (Table 1). One of the ceramic samples, labelled as SiC$_{50}$-7, was processed from SiC nanopowders of 50 nm of particle size (Nanostructures & Amorphous Materials Inc., USA, polytype 3C) containing 5 wt.% of Y$_2$O$_3$ and 2 wt.% of Al$_2$O$_3$, both used as sintering additives. The scaffold was sintered at 1700 °C for 5 min in Ar atmosphere (6 Pa of pressure) using the Spark Plasma Sintering (SPS) technique without applying any mechanical pressure [19]. The MAX-phase specimen was printed from 98% pure Cr$_2$AlC MAX lab-synthesised powders [25] and densified by pressureless SPS at 1200 °C for 10 min in Ar [20].

The so-called rGO-PSZ scaffold was obtained by printing graphene oxide nanoplatelets (GO, N002-PDE Angstron Materials Inc., USA, 2–3 nm thick and lateral size in the x-y plane ≤ 7 μm). The GO printed sample was reduced at 1200 °C in nitrogen atmosphere inside a graphite furnace and, subsequently, vacuum infiltrated with a liquid organic-polysilazane (PSZ, a preceramic polymer of Si, C, H, N) and treated at 200 °C in a tubular electric furnace under a continuous nitrogen flow for polymer crosslinking [7]. The skeleton consisted of 93 and 7 wt% of crosslinked PSZ and rGO, respectively. Fig. 2 illustrates representative rod microstructures of the three selected specimens.

3.2. Thermal conduction testing

The proposed experimental setting is based on the steady-state unidirectional heat flow and is of advantage, particularly, when thermocouples are difficult to place in the sample. The scheme of the device is presented in Fig. 3a. It consists of two Peltier cells respectively acting as heater and cooler plates that allow stabilizing temperature differences of ~50 °C between the hot (~60 °C) and cold (~5 °C) plates. Two cylinders (15 mm in diameter and 45 mm in height) of copper with high thermal conductivity (~400 W m^{-1} K^{-1}) were placed in contact to the heater and cooler devices to improve the heat diffusion, while the test sample was set in between. In some tests, additional stainless steel (AISI 310, labelled
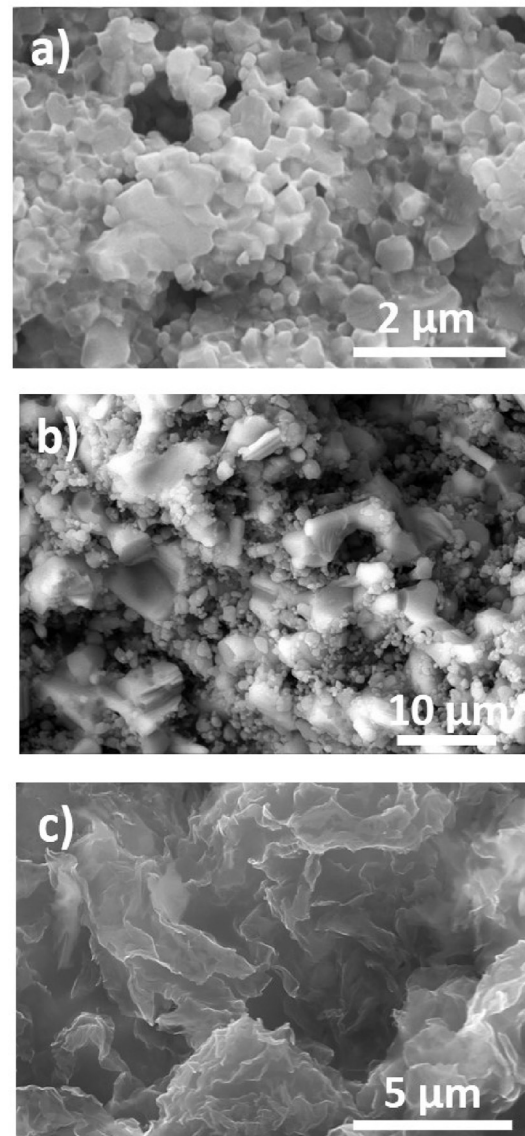

Fig. 2. SEM images of the fracture surface of rods corresponding to the 3D specimens of: SiC$_{50}$-7 (a), MAX-phase (b), and rGO-PSZ (c). (a) From Refs [19].

Table 1

Dimensions of the 3D printed specimens including D (square side in the x-y plane) and Z (height); and their characteristic densities (theoretical –Th-, geometric –Geo- and that of the rod -Rod) and porosities (total, rod and macro).

3D-specimen	dimensions (mm)		density (g·cm^{-3})			porosity (%)		
	D	Z	Th	Geo	Rod	Total	Rod	Macro
SiC$_{50}$-7	11.6	4.6	3.3	1.1	2.7	67	23	59
MAX-phase	10.2	5.0	5.2	2.2	3.8	60	24	44
rGO – PSZ	11.6	4.7	1.14	0.4	1.1	65	24	54

as AISI) cylinders (15 mm in diameter and 10 mm height) of lower thermal conductivity (~16 W m^{-1} K^{-1}) were introduced between the sample and the Cu cylinders to increase the excessively small gradients achieved just with Cu (~0.03 °C·pixel^{-1}). The metal pieces in contact with the specimen, either Cu or AISI, were used as control samples in the measurement of the thermal gradients. The problem sample should have a section similar to that of the control samples. The whole measurement system (cylinder/specimen/cylinder) was thermally insulated to prevent heat losses and induce uniaxial heat flow. A vertical slot (~5 mm wide)
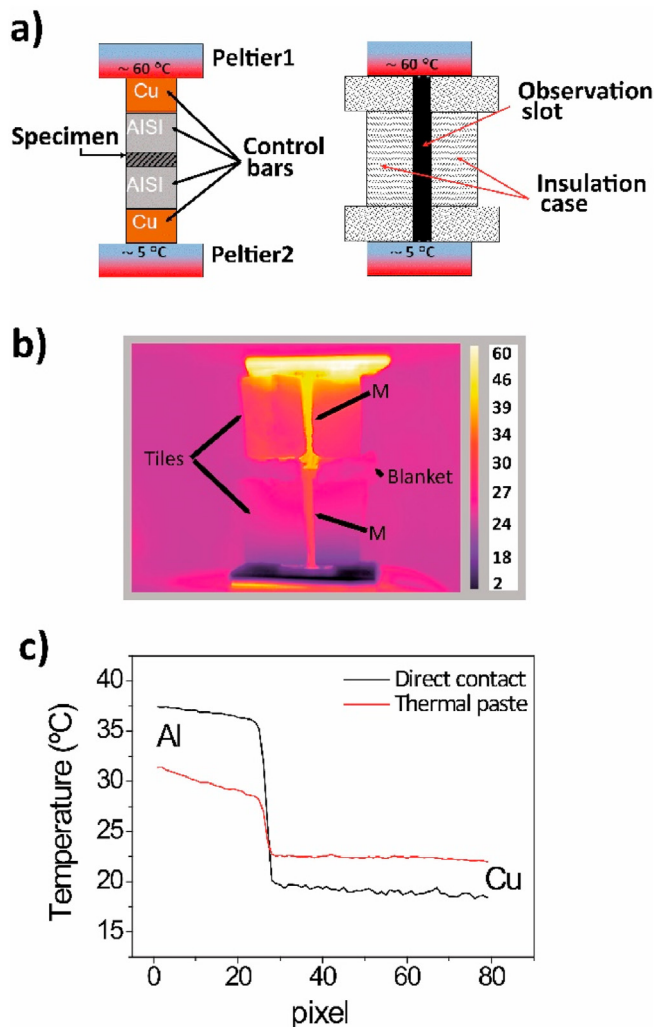
Fig. 3. (a) Schematic of the thermal conductivity measurement system showing the stacking of the heating and cooling Peltier elements, the control bars and the specimen (on the left) and the thermal insulation case with the observation slot (on the right). (b) Thermal image of a test with two metallic control cylinders (both labelled as M), using fiberglass tiles (at top and bottom) and a fiberglass blanket (central measurement area) for the insulating case (temperature scale is in °C). (c) Temperature profiles along the heat flow direction for an aluminium/copper assembly without (direct contact) and with thermal paste applied at the contact.

was machined in the insulation case along the thermal flow direction (Fig. 3a) to measure the surface temperature of the samples with a high resolution infrared camera (FLIR A325 SC, USA), as the attachment of the thermocouples in the present case was a challenging task. The exposed sample surface was coated with graphite to eliminate errors associated with differences in the emissivity between the samples and the control metal cylinders. The camera captures the radiation over the wavelength range of 8–12 μm and generates thermographic images from the temperature distribution; its resolution is 320 × 240 pixels and the accuracy is ±2%. Two types of lenses were used, the standard lens of 18 mm (25°) and the close-up lens (IFOV 50 μm optics) suitable for observations at higher magnification (macro lens). The observation distance was 25 cm for the standard lens and 2 cm for the macro one.

Different fiberglass materials were used for the thermal insulation, in particular, rigid tiles and a flexible blanket, the latter with a thermal conductivity of ~0.04 W m^{-1} K^{-1} at room temperature, which is much lower than that of the tiles (~0.1 W m^{-1} K^{-1}). The thermal image shown in Fig. 3b corresponds to a test in which insulating fiberglass tiles were

Table 2

Temperature gradients (∇T) measured for the Pyroceram®, Pyrex® and alumina dense materials, as well as for the control metal cylinder in each test; and thermal conductivity calculated using the stainless steel ($\kappa_{s,AISI}$) and data for the Pyroceram® run ($\kappa_{s,Pyroceram}$) previously normalized using Eq. (3) as references. Certified thermal conductivity values and average temperatures ($T_{average}$) are also included.

Test (certified κ)	Material ($T_{average}$)	∇T (°C·Pixel^{-1})	$\kappa_{s,\,AISI}$(W m^{-1} K^{-1})	$\kappa_{s,Pyroceram}$ (W m^{-1} K^{-1})
Pyroceram® (4.1 W m^{-1} K^{-1})	AISI (37 °C) specimen (21.5 °C)	0.13 1.42	1.5	–
Pyrex® (1.1 W m^{-1} K^{-1})	AISI (55 °C) specimen (33 °C)	0.05 2.07	0.4	1.15
Alumina (33.0 W m^{-1} K^{-1})	AISI (30 °C) specimen (21.5 °C)	0.12 0.16	12.3	33.50

used for the top and bottom regions of the stacking; whereas a fiberglass blanket was employed for the central measurement area. It is evident that while the blanket adequately insulates the sample, being undistinguishable from the environment in the thermal image, the tile-covered regions exhibit considerable heat losses, since they display distinct temperatures from that of the surrounding; specifically, the upper part shows a temperature ~7 °C above the room temperature and the lower part is ~1.5 °C below. Therefore, the flexible insulation fiberglass blanket was preferred for thermally shielding the measurement area.

As can be seen in Fig. 3c, the contact thermal resistance between the different materials led to important temperature drops at the interface (~20 °C in the case of aluminium and copper cylinders). Accordingly, a high thermal conductivity thermal paste (RS®, 503-357 ZP, 2.9 W m^{-1} K^{-1}, which contains Ag particles) was applied to all interfaces. The use of the thermal paste ensures better heat transfer by conduction between the two materials, decreasing the temperature drop to just 5 °C (75% reduction) in the case of aluminium and copper bars (Fig. 3c).

4. Results

4.1. Dense standard specimens

The unknown conductivity of the sample (κ_s) can be calculated by comparing the gradient measured along it (∇T_s) with that of a reference material (∇T_{ref}) of known thermal conductivity (κ_{ref}) using the expression:

$$\kappa_s = \kappa_{ref} \cdot \frac{\nabla T_{ref}}{\nabla T_s} \qquad (2)$$

Temperature gradients (in °C·pixel^{-1}) measured for the Pyroceram®, Pyrex® and alumina standards, as well as for the control stainless steel bar, are collected in Table 2. In the absence of heat losses, the stainless steel bar (κ = 16.3 W m^{-1} K^{-1}) can be used as reference material. The application in this case of the Eq. (2) provided thermal conductivity values ~ 65% lower ($\kappa_{s,\,AISI}$ equals to 0.4, 1.5 and 12.3 W m^{-1} K^{-1} for Pyrex®, Pyroceram® and alumina, respectively, as shown in Table 2) than those certificated for the three reference materials (κ of 1.1, 4.1 and 33.0 W m^{-1} K^{-1}, respectively). Therefore, the heat losses through the observation slot, inevitable in the proposed design, are not negligible. Another option was, then, proposed to determine the thermal conductivity of the samples in a more accurate way. It consisted in comparing gradients obtained in two different tests for the specimen of unknown thermal conductivity (s test) and the reference material (ref test), both specimens having the same dimensions. To do that correctly, gradients should be firstly normalized by dividing them by the ratio "C" between the gradients along the AISI cylinders in both tests, for the sample (s subscript) and reference (ref subscript):

Table 3

3D specimens thermally analysed indicating the testing orientation, metal cylinders, average temperature, observation lens and temperature gradient (∇T). Gradients are not the same for both lenses because the observation distances are different.

Orientation	Metal cylinders	Specimen	T (°C)	Lens	∇T (°C·pixel^{-1})
Longitudinal	Cu	rGO-PSZ	25.3	Standard	1.92
				Macro	0.12
	Cu	SiC$_{50}$-7	26.8	Standard	0.49
				Macro	0.04
	AISI	SiC$_{50}$-7	25.9	Standard	0.31
				Macro	0.06
	AISI	MAX-phase	27.3	Standard	0.64
				Macro	0.14
	AISI	rGO-PSZ	23.3	Standard	2.00
Transverse	Cu	rGO-PSZ	31.2	Standard	3.24
				Macro	0.35
	Cu	SiC$_{50}$-7	26.0	Standard	0.57
				Macro	0.03
	AISI	MAX-phase	33.3	Standard	0.81
				Macro	0.16

$$C = \frac{\nabla T_{AISI,\,s}}{\nabla T_{AISI,\,ref}} \qquad (3)$$

so that temperature gradients measured for the AISI bars would be equal in both tests.

The Pyroceram® test was used as the reference to evaluate the thermal conductivity of Pyrex® and alumina. Introducing the normalized gradients for the unknown-κ sample and corrected data of ∇T_{ref} and κ_{ref} for Pyroceram® in Eq. (2), the deduced thermal conductivity values (labelled as $\kappa_{s,Pyroceram}$ in Table 2) for Pyrex® and alumina were close to the certified data, with differences of less than 3%, which validates this procedure.

4.2. Porous 3D printed specimens

Table 3 shows data for the porous 3D samples tests. These structures were analysed in two orthogonal directions, referred to as longitudinal and transverse, which corresponded to IR camera focusing on the patterned surface (heat flowing along the x-y plane) or on one frame lateral surface (heat flux in z-direction), respectively, as indicated in Fig. 4a. In addition, observations were made using both types of lens, standard and macro. A relevant result is the anisotropy observed in the heat flow as higher thermal gradients were measured for the transverse orientation, which would indicate a lower thermal conductivity in the z-direction, i.e. perpendicularly to the plane in which the rods are aligned. A comparable anisotropy has also been confirmed for the electrical conductivity in similar structures of different materials, such as SiC, graphene nanoplatelets (GNP), and SiC-GNP composites [24,26].

The plot of Fig. 4b shows an increased temperature gradient when moving from SiC$_{50}$-7 > MAX-phase > rGO-PSZ structures. It should be noted that the observed tendency cannot be linked to the specimen porosity, neither the macro-porosity nor the rod porosity. In particular, although the three specimens have similar macro-porosities, being in the range of 44–55%, and also the same rod porosity of ~24% (Table 1), significant differences in gradients are evidenced, which imply that SiC$_{50}$-7 and MAX-phase structures would be ~4 times more conductive than rGO-PSZ one. The ratio between the longitudinal and transverse gradients, which gives an idea of the anisotropy, varies from 1.1 for the SiC$_{50}$-7 structure to ~1.7 for the rGO-PSZ one.

Data represented in Fig. 4b corresponds to the standard lens, since large temperature fluctuations were observed with the macro lens. Fig. 5a displays some representative examples of thermal images and temperature profiles for 3D printed specimens when observing the x-y plane, i.e. the longitudinal orientation. As seen, the temperature distribution allows perceiving the rods and macro-pores in the x-y plane (IR
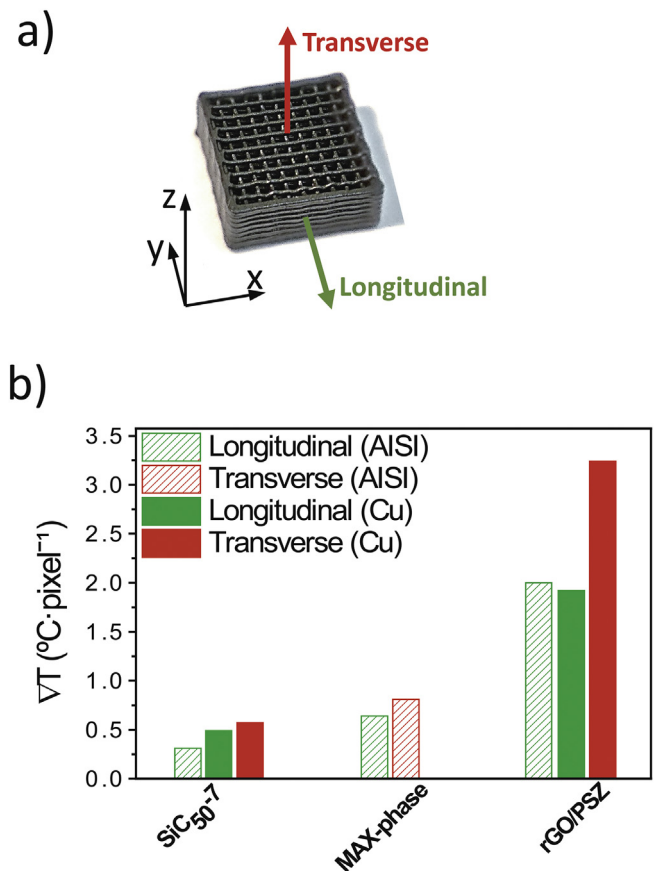

Fig. 4. (a) Heat flow direction in the tests for the longitudinal and transverse orientations and (b) bar diagram showing the increasing gradients measured for the 3D materials of similar patterned structure in the different testing conditions shown in the legend.

images in Fig. 5a), and also periodic fluctuations in the temperature profiles induced by the macro-porosity inherent to these printed designs.

The heterogeneities associated with the presence of hollow cells and rods along the profile are better appreciated with the macro lens than with the standard ones (see the two temperature profiles for the MAX-phase structure in Fig. 5a) due to the greater number of data recorded per cm (5 times more than the standard lens). On the other hand, tests carried out on a rGO-PSZ structure levelled by gently grinding showed that, although the profiles considerably flatten (even the profile along a rod is practically linear), local temperature drops associated with the macro-pores were still observed.

On the other hand, the thermal conductivity of the metallic bars also affected data. Thus, tests carried out with the copper cylinders in direct contact with the specimen, without intercalating steel cylinders, gave some problems, especially for the highly porous samples. As it can be seen in Fig. 5b for the rGO-PSZ sample, using the copper cylinders strongly altered the temperature profiles perpendicular to the heat flow, since they were not flat except in the central zone, changing from convex to concave when moving away from the heat source. That is, in the upper zone, higher temperatures were measured at the centre than at the lateral edges close to the insulating case, while in the lower zone, the temperatures at the centre were lower than at sides. Thus, it seems that the camera was somehow capturing the temperature of the top and bottom metal controls. In fact, when steel cylinders, with a much lower conductivity than copper (16 versus 400 W m^{-1} K^{-1}, at room temperature), were placed between the copper and the test specimen, the curvature significantly reduced, particularly at the lower part of the sample, as shown in Fig. 5b.

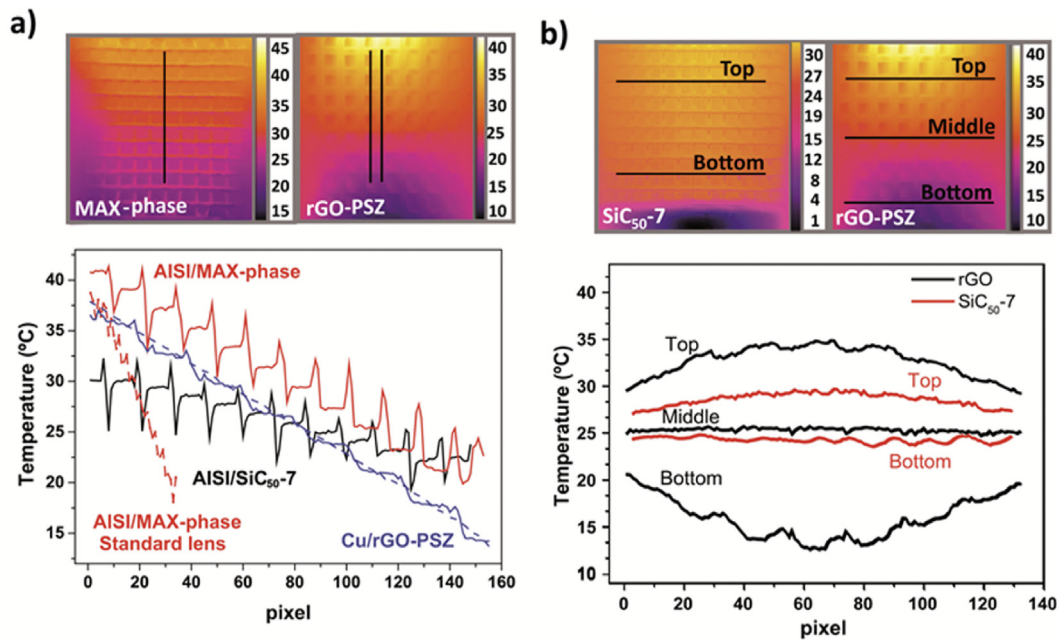The effective thermal conductivity without considering the heat

Fig. 5. Thermal images of the x-y patterned surface (macro lens data) for the longitudinal orientation and plots of the temperature profiles along the lines depicted in the IR images of (a) and (b), corresponding to directions aligned with (a) and perpendicular to (b) the heat flow, respectively, and for different 3D materials. Profile generated with the standard lens for the MAX-phase structure (dashed red line) is also included in (a) plot for comparison. Two profiles are included for the grinded rGO-PSZ in plot (a): one through the macro-pores (continuous line) and another taken along a rod (dashed line). Temperature profiles in (b) were recorded at different distances from the heat source (marked on the thermographic images of (b)) for the Cu/rGO-PSZ and AISI/SiC$_{50}$-7 arrangements. The small temperature variations are linked to the macro-pores. (For interpretation of the references to colour in this figure legend, the reader is referred to the Web version of this article.)

transfer by convection and radiation of this type of structure for the two orientations analysed, that is, longitudinal (κ_L), along the plane of crisscross rods, and transverse (κ_T), perpendicular to that plane, can be estimated from the conductivity of the rod (κ_{rod}) using a simple model of thermal resistors [24]:

$$\kappa_L = \frac{\varnothing}{2a}\kappa_{rod} \qquad (4)$$

$$\kappa_T = \frac{h\varnothing}{a^2}\left(1 - \frac{h}{2\varnothing}\right)\cdot\kappa_{rod} \qquad (5)$$

and introducing the parameters that define the structure, $\varnothing$, a and h (Fig. 1a), which are collected in Table 4 for each of the three tested materials. As the factors that multiply κ_{rod} in the Eqs. (4) and (5) are similar for the three specimens (~0.17 and ~0.04, respectively), the effective conductivity would exclusively depend on κ_{rod}, which is strongly affected by π_{rod} and the intrinsic conductivity of the material. From the data collected in Table 4, it is deduced that the κ_L/κ_T ratio was ~4, higher than the anisotropy estimated from the corresponding gradients ratio (<2 as shown in Table 3). This can be explained by the contribution of the structure frame in both orientations, which has not been taken into account in the resistors model. The frame contribution to thermal conductivity in the longitudinal and transverse orientations was calculated in S1 section of the supplementary information. As seen, it affects differently to κ_L and κ_T, reducing the anisotropy to values ranging between 1.3 and 1.9, both closer to those deduced from the gradient ratios.

Values for κ_{rod} in Table 4 were estimated from the thermal conductivity of dense materials (κ_0) corrected by the rod porosity using Pabst-Gregorova's exponential relation [27]. In the case of the SiC$_{50}$-7 and MAX-phase dense specimens, κ_0 was measured by the laser flash method (30 and 16 W m^{-1} K^{-1}, respectively). For the rGO-PSZ specimen a κ_0 of 9 W m^{-1} K^{-1} was estimated from the rGO and PSZ volumen fractions considering both rGO and PSZ as continuos phases, and thermal conductivities of 400 W m^{-1} K^{-1} for the rGO (see calculation in S2 section)

and 1 W m^{-1} K^{-1} for the cross-linked polymer. After κ_0 was corrected by the rod porosity, κ_{rod} values included in Table 4 were inferred, which indicates that the conductivity of the SiC$_{50}$-7 structure would be ~2 and 3 times higher than that of the MAX-phase and rGO-PSZ structures, respectively. This fact agrees with the experimental observations when comparing their gradients under similar conditions (i.e. same metal controls). Thus, the gradient measured in the specimen for the Cu/rGO-PSZ test is 4 times larger than that measured for SiC$_{50}$-7 and, accordingly, that measured for the AISI/MAX-phase system is 3 times higher than that measured for AISI/SiC$_{50}$-7 (Fig. 4b and Table 3). Although to get absolute values of κ, a standard test would be necessary (a structure of identical dimensions to those tested and of certified thermal conductivity), these results demonstrate that the proposed method offers reasonably data in a comparative way that allow predicting the thermal behaviour of the macroporous structures. This procedure also has the crucial advantage that using thermocouples is unnecessary. The correlation between the measured thermal gradients and the thermal conductivity estimated for the structures is shown in Fig. 6, where data were fitted with $\nabla T = A \cdot \kappa^{-x}$ being x = 1.3.

Finally, the thermal conductivities of the structures tested with the AISI bars were estimated applying the procedure described in section 4.1, that is, comparing the normalized gradients using Eq. (3) and the test with Pyroceram® as a reference, as it was done with the dense materials. Thus, the conductivity of the MAX-phase structure was estimated in 3.4 and 2.2 W m^{-1} K^{-1} for the longitudinal and transverse directions, respectively, the ratio between them being 1.6; while for the SiC$_{50}$-7 and the rGO-PSZ structures, a longitudinal conductivity of 3.0 and 0.5 W m^{-1} K^{-1}, respectively, was obtained. These values, although somewhat differing, are consistent with those deduced from the resistors model considering the contribution of the frames (Table 4). There are several factors that can explain the observed discrepancies, like errors due to: i) changes in the heat flow associated with the cross section differences between the metal bars (176 mm^2) and the porous 3D specimens (~125 and ~50 mm^2 for the front and lateral configurations, respectively, according to the data in Table 1), which would induce lateral heat losses; ii)

Table 4

Parameters of the 3D structures (diameter, "Ø", in-plane distance between rods, "a", distance between parallel rods in z-direction, "h"), estimated rod thermal conductivity (κ_{rod}) effective thermal conductivity in the longitudinal (κ_L) and transversal (κ_T) directions deduced from the resistors model (Eq. (4) and (5)) and corresponding values including the frame contribution. The experimentally estimated (Exp) values are also included.

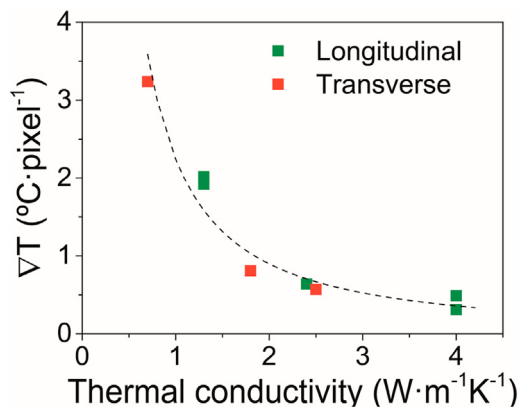| Material	Ø (μm)	a (μm)	h (μm)	Thermal conductivity (W m^{-1} K^{-1})					
				k_{rod}	k_L Eq. (4)	k_T Eq. (5)	k_L Frame	k_T Frame	k_L Exp
SiC$_{50}$ – 7 [19]	210	690	360	19.2	2.9	0.7	4.0	2.5	3.0
MAX-phase [20]	265	760	415	10.0	1.7	0.4	2.4	1.8	3.4
rGO-PSZ [7]	345	1010	540	5.6	1.0	0.2	1.3	0.7	0.5

Fig. 6. Temperature gradients as a function of the thermal conductivity estimated for SiC$_{50}$-7, MAX-phase and rGO-PSZ structures (data included in Table 4). Curve is the data fit with $\nabla T = A \cdot K^{-x}$.

the use of an inappropriate reference test that corresponded to a dense specimen of different geometry and size; iii) the large temperature variations associated with the presence of the macro-pores and rods that can also affect the measured gradients; and finally, iv) a contribution of the convection and radiation heat transfer that has not been taken into account in the resistors model. It should be pointed out that, in this method, the thermal resistances linked to contacts would not have influence in the measurement of the temperature gradients, as the use of the IR camera allows perfectly their discrimination.

5. Conclusions

The proposed approach to estimate the thermal conductivity of macroporous materials based on high resolution infrared thermography allows determining temperature gradients and perfectly discerning thermal resistances linked to contacts while avoiding the use of thermocouples, as attaching thermocouples to 3D porous structures developed by direct ink writing results quite a challenge. Temperature fluctuations associated with the reticulated structure are perfectly reproduced along the thermal profile recorded when using the macro lens. An excellent correlation between the measured temperature gradients and the thermal conductivity of the 3D structures, estimated from a simple resistors model, is established. Thermal gradients determined in two orthogonal directions, corresponding to IR observations of the rod lattice (heat flowing along the x-y plane) and the lateral frame (heat flux in z-direction), support the result of an anisotropic thermal conductivity with an anisotropy factor <2 for this type of structure.

Declaration of competing interest

The authors declare that they have no known competing financial interests or personal relationships that could have appeared to influence the work reported in this paper.

Appendix A. Supplementary data

Supplementary data to this article can be found online at https ://doi.org/10.1016/j.oceram.2020.100028.

References

[1] T.D. Ngo, A. Kashani, G. Imbalzano, K.T. Nguyen, D. Hui, Additive manufacturing (3D printing): a review of materials, methods, applications and challenges, Compos, Part B-Eng 143 (2018) 172–196, https://doi.org/10.1016/j.compositesb.2018.02.012.

[2] Z. Chen, Z. Li, J. Li, C. Liu, C. Lao, Y. Fu, C. Liu, Y. Pi, P. Wang, Y. He, 3D printing of ceramics: a review, J. Eur. Ceram. Soc. 39 (2019) 661–687, https://doi.org/10.1016/j.jeurceramsoc.2018.11.013.

[3] A. Quintanilla, J.A. Casas, P. Miranzo, M.I. Osendi, M. Belmonte, 3D-Printed Fe-doped silicon carbide monolithic catalysts for wet peroxide oxidation processes, Appl. Catal. B Environ. 235 (2018) 246–255, https://doi.org/10.1016/j.apcatb.2018.04.066.

[4] A. Quintanilla, J. Carbajo, J.A. Casas, P. Miranzo, M.I. Osendi, M. Belmonte, Graphene-based nanostructures as catalysts for wet peroxide oxidation treatments: from nanopowders to 3D printed porous monoliths, Catal. Today 356 (2020) 197–204. https://doi.org/10.1016/j.cattod.2019.06.026, 2019.

[5] Y. Tang, W. Zhou, M. Pan, H. Chen, W. Liu, H. Yu, Sintered Porous Copper Fiber Felts: an innovative methanol vapor reformer catalytic support for hydrogen production, Int. J. Hydrogen Energy 33 (2008) 2950–2956, https://doi.org/10.1016/j.ijhydene.2008.04.006.

[6] Y. Li, Z.Y. Fu, B.L. Su, Hierarchically structured porous materials for energy conversion and storage, Adv. Funct. Mater. 22 (2012) 4634–4667, https://doi.org/10.1002/adfm.201200591.

[7] J.J. Moyano, J. Mosa, M. Aparicio, D. Pérez-Coll, M. Belmonte, P. Miranzo, M.I. Osendi, Strong and light cellular silicon carbonitride–Reduced graphene oxide material with enhanced electrical conductivity and capacitive response, Addit. Manuf 30 (100849) (2019), https://doi.org/10.1016/j.addma.2019.100849.

[8] U. Scheithauer, E. Schwarzer, T. Moritz, A. Michaelis, Additive manufacturing of ceramic heat exchanger: opportunities and limits of the lithography-based ceramic manufacturing (LCM), J. Mater. Eng. Perform. 27 (2018) 14–20, https://doi.org/10.1007/s11665-017-2843-z.

[9] M. Pelanconi, M. Barbato, S. Zavattoni, G.L. Vignoles, A. Ortona, Thermal design, optimization and additive manufacturing of ceramic regular structures to maximize the radiative heat transfer, Mater. Des. 163 (107539) (2019), https://doi.org/10.1016/j.matdes.2018.107539.

[10] S.Y. Chung, d. Stepahn, M. Abd Elrahman, T.S. Han, Effects of anisotropic voids on thermal properties of insulating media investigated using 3D printed samples, Construct. Build. Mater. 111 (2016) 529–542, https://doi.org/10.1016/j.conbuildmat.2016.02.165.

[11] C. Shemelya, A. de la Rosa, A.R. Torrado, K. Yu, J. Domanowski, P.J. Bonacuse, R.E. Martin, M. Juhasz, F. Hurwitz, R.B. Wicker, B. Conner, E. MacDonald, D.A. Roberson, Anisotropy of thermal conductivity in 3D printed polymer matrix composites for space based cube satellites, Addit. Manuf 16 (2017) 186–196, https://doi.org/10.1016/j.addma.2017.05.012.

[12] T. Flaata, G.J. Michna, T. Letcher, Thermal Conductivity Testing Apparatus for 3D Printed Materials, Proceed, ASME, Summer Heat Transfer Conference, Washington, USA, 2017.

[13] H. Prajapati, D. Ravoori, R.L. Woods, A. Jain, Measurement of anisotropic thermal conductivity and inter-layer thermal contact resistance in polymer fused deposition modelling (FDM), Addit. Manuf 21 (2018) 84–90, https://doi.org/10.1016/j.addma.2018.02.019.

[14] D. Ravoori, L. Alba, H. Prajapati, A. Jain, Investigation of process-structure-property relationships in polymer extrusion based additive manufacturing through in situ

high speed imaging and thermal conductivity measurements, Addit. Manuf 23 (2018) 132–139, https://doi.org/10.1016/j.addma.2018.07.011.

[15] A. Elkholy, M. Rouby, R. Kempers, Characterization of the anisotropic thermal conductivity of additively manufactured components by fused filament fabrication, Prog. Addit. Manuf 4 (2019) 497–515, https://doi.org/10.1007/s40964-019-00098-2.

[16] N.B. Vargaftik, L.P. Filippov, A.A. Tarzimanov, E. E Totskii, Handbook of thermal conductivity of liquids and gases, first ed., CRC press, Moscow (Russia), 1994, ISBN 0-8493-9345-0.

[17] D. Zhao, X. Qian, X. Gu, S.A. Jajja, R. Yang, Measurement techniques for thermal conductivity and interfacial thermal conductance of bulk and thin film materials, J. Electron. Packag. 138 (2016), 040802, https://doi.org/10.1115/1.4034605.

[18] A. Palacios, L. Cong, M.E. Navarro, Y. Ding, C. Barreneche, Thermal conductivity measurement techniques for characterizing thermal energy storage materials–A review, Renew. Sustain. Energy Rev. 108 (2019) 32–52, https://doi.org/10.1016/j.rser.2019.03.020.

[19] A. Gómez-Gómez, J.J. Moyano, B. Román-Manso, M. Belmonte, P. Miranzo, M.I. Osendi, Highly-porous hierarchical SiC structures obtained by filament printing and partial sintering, J. Eur. Ceram. Soc. 39 (2019) 688–695, https://doi.org/10.1016/j.jeurceramsoc.2018.12.034.

[20] M. Belmonte, M. Koller, J.J. Moyano, H. Seiner, P. Miranzo, M.I. Osendi, J. González-Julián, Multifunctional 3D printed cellular MAX-phase architectures, Adv. Mat. Technol 4 (1900375) (2019), https://doi.org/10.1002/admt.201900375.

[21] J.J. Moyano, I. García, J.J. de Damborenea, D. Pérez-Coll, M. Belmonte, P. Miranzo, M.I. Osendi, The remarkable effects of an electrodeposited copper skin on the strength, and the electrical and thermal conductivities of reduced graphene oxide printed scaffolds, ACS Appl. Mater. Interfaces 12 (2020) 14209–24217, https://doi.org/10.1021/acsami.0c01819.

[22] M. Belmonte, G. Lopez-Navarrete, M.I. Osendi, P. Miranzo, Heat dissipation in 3D printed cellular aluminum nitride structures, J. Eur. Ceram. Soc. sent for publication. Ref. JECS-D-20-01963 (2020) 20–1963.

[23] J. Lewis, Direct ink writing of 3D functional materials, Adv. Funct. Mater. 16 (2006) 2193–2204, https://doi.org/10.1002/adfm.200600434.

[24] B. Román-Manso, F.M. Figueiredo, B. Achiaga, R. Barea, D. Pérez-Coll, A. Morelos-Gómez, M. Terrones, M.I. Osendi, M. Belmonte, P. Miranzo, Electrically functional 3D-architectured graphene/SiC composites, Carbon 100 (2016) 318–328, https://doi.org/10.1016/j.carbon.2015.12.103.

[25] J. Gonzalez-Julian, S. Onrubia, M. Bram, O. Guillon, Effect of sintering method on the microstructure of pure Cr_2AlC MAX phase ceramics, J. Ceram. Soc. Jpn. 124 (2016) 415–420, https://doi.org/10.2109/jcersj2.15263.

[26] G. de la Osa, D. Pérez-Coll, P. Miranzo, M.I. Osendi, M. Belmonte, Printing of graphene nanoplatelets into highly electrically conductive three-dimensional porous macrostructures, Chem. Mater. 28 (2016) 6321–6328, https://doi.org/10.1021/acs.chemmater.6b02662.

[27] W. Pabst, T. Uhlířová, E. Gregorová, A. Wiegmann, Young's modulus and thermal conductivity of model materials with convex or concave pores – from analytical predictions to numerical results, J. Eur. Ceram. Soc. 38 (7) (2018) 2694–2707, https://doi.org/10.1016/j.jeurceramsoc.2018.01.040.